

# Reductive dissolution of biogenic magnetite

Toshitsugu Yamazaki (✉ [yamazaki@aori.u-tokyo.ac.jp](mailto:yamazaki@aori.u-tokyo.ac.jp))

---

## Express Letter

**Keywords:** biogenic magnetite, magnetofossil, reductive diagenesis, FORC diagram

**Posted Date:** September 16th, 2020

**DOI:** <https://doi.org/10.21203/rs.3.rs-50707/v2>

**License:** © ⓘ This work is licensed under a Creative Commons Attribution 4.0 International License.

[Read Full License](#)

---

**Version of Record:** A version of this preprint was published on October 17th, 2020. See the published version at <https://doi.org/10.1186/s40623-020-01290-3>.

# Abstract

Reductive dissolution of magnetite is known to occur below the Fe-redox boundary in sediments. In this study detailed processes associated with biogenic magnetite dissolution are documented. A sediment core from the Japan Sea was used for this purpose, in which reductive dissolution of magnetic minerals is known to start at depths of about 1.15 m and is mostly complete within a depth interval of about 0.35 m. Using first-order reversal curve diagrams, preferential dissolution of biogenic magnetite within this interval is estimated from the observation that a narrow peak that extends along the coercivity axis (central ridge), which is indicative of biogenic magnetite, diminishes downcore. Transmission electron microscopy is used to demonstrate that the sediments contain three magnetofossil morpho-types: octahedra, hexagonal prisms, and bullet-shaped forms. Within the reductive dissolution zone, partially etched crystals are commonly observed. With progressive dissolution, the proportion of bullet-shaped magnetofossils decreases, whereas hexagonal prisms become more dominant. This observation can be explained by the differences in resistance to dissolution among crystal planes of magnetite and the differences in surface area to volume ratios. Magnetofossil morphology may reflect the preference of magnetotactic bacterial lineages for inhabiting specific chemical environments in sediments. However, it could also reflect alteration of the original morphological compositions during reductive diagenesis, which should be considered when using magnetofossil morphology as a paleoenvironmental proxy.

## Introduction

It is important to understand magnetic mineral diagenesis after deposition of sediments to constrain interpretation of paleomagnetic records and of paleoenvironments using rock-magnetic proxies (e.g. Roberts 2015). Associated with organic matter degradation, reduction from  $\text{Fe}^{3+}$  to  $\text{Fe}^{2+}$  begins after sequential progression of aerobic respiration, nitrate reduction, and manganese reduction. Below the Fe-redox boundary, where iron reduction starts, magnetic mineral dissolution may occur. The depth of the Fe-redox boundary in a sediment column varies from zero to tens of meters or more below the seafloor depending on various factors, including organic-carbon influx and bottom-water oxygen content. Reductive dissolution of magnetic minerals has been reported widely from various sediments (e.g. Karlin and Levi 1983; Canfield and Berner 1987; Yamazaki et al. 2003; Rowan et al. 2009; Korff et al. 2016). As reduction continues, sediments undergo sulphidic diagenesis and iron sulfide minerals like greigite and pyrite grow within the sediments (Rowan et al. 2009; Roberts 2015).

It is now recognized widely that biogenic magnetite is a major constituent of magnetic mineral assemblages in marine sediments that have not undergone reductive diagenesis (Roberts et al. 2011, 2012, 2013; Yamazaki and Ikehara 2012; Yamazaki and Shimono 2013). Biogenic magnetite may, thus, play an important role in sedimentary remanent magnetization acquisition (Kirschvink 1982; Ouyang et al. 2014; Chen et al. 2017). In addition, magnetofossil morphology may be a proxy for past sediment chemical conditions (Hesse 1994; Yamazaki and Kawahata 1998; Chang et al. 2018; Yamazaki et al. 2019). Biogenic magnetite undergoes reductive dissolution like magnetic minerals of other origins, and biogenic magnetite is inferred to be lost earlier than other magnetite types because of its finer grain sizes

(Karlin 1990). Reductive dissolution of biogenic magnetite should influence paleomagnetic and paleoenvironmental interpretation, but the details of the dissolution processes have not been reported so far.

The purpose of this study is to document dissolution processes of biogenic magnetite during reductive diagenesis based on first-order reversal curve (FORC) diagrams and transmission electron microscope (TEM) observations. We discuss differences in resistance to reductive diagenesis depending on magnetofossil morphology.

## Materials And Methods

Sediment core GH98-1232 from the northern part of the Japan Sea at 44°48.09'N, 139°41.97'E was used for this study (Fig. 1). The water depth of the coring site is 838 m, and the present-day Fe-redox boundary occurs a few centimeters below the sediment-water interface, which is recognized from a brown-to-gray change in sediment color. A rock-magnetic study by Yamazaki et al. (2003) revealed that reductive dissolution of magnetic minerals starts at depths of about 1.15 m in this core and is mostly completed within an interval of about 0.35 m (Fig. 2). Magnetic concentration-dependent parameters decrease rapidly downcore within this interval with the anhysteretic remanent magnetization (ARM) decreasing first, followed by the saturation isothermal remanent magnetization (SIRM), and then the low-field magnetic susceptibility. Average magnetic grain size estimated from the ratio of ARM susceptibility ( $k_{\text{ARM}}$ ) to SIRM rapidly increases downcore from 1.18 to 1.35 m, which indicates that finer magnetic grains are lost before larger grains. Average magnetic grain size then decreases a little between 1.35 and 1.6 m. Based on S-ratio and low-temperature measurements, magnetite dominates the magnetic mineral assemblage of surface sediments to the depth which dissolution initiates, and the relative proportion of high-coercivity minerals (e.g., hematite) increases with depth as magnetite dissolves preferentially in this interval (Yamazaki et al. 2003).

### FORC diagrams

FORC diagrams are used widely in rock magnetism to elucidate the distribution of coercivities ( $H_c$ ) and magnetostatic interactions ( $H_{ij}$ ) within magnetic particle assemblages, from which information on domain states, grain sizes and shapes, mineralogy, and spatial distribution of constituents can be obtained (e.g. Pike et al. 1999; Roberts et al. 2000, 2014). FORC diagrams are particularly useful for detecting biogenic magnetite in sediments; intact chains of biogenic magnetite behave as isolated non-interacting single-domain (SD) grains, which produce a characteristic narrow peak that extends along the coercivity axis at zero interaction field on a FORC diagram, called the “central ridge” (Egli et al. 2010; Li et al. 2012; Roberts et al. 2012; Yamazaki and Ikehara 2012; Chang et al. 2014).

FORC measurements were conducted at ~5 cm stratigraphic intervals within and near the magnetic-mineral dissolution zone using an alternating-gradient magnetometer (Princeton MicroMag 2900) at the Geological Survey of Japan (GSJ), National Institute of Advanced Industrial Science and Technology

(AIST). A total of 167 FORCs were measured for each sample, with  $H_c$  between 0 and 100 mT,  $H_u$  between -50 and 50 mT, and field spacing of approximately 1.3 mT. The maximum applied field was 1.0 T, and the averaging time for each measurement point was 200 ms. The FORCinel software (Harrison and Feinberg 2008, version 3.05 in 2019) was used to produce diagrams, and the VARIFORC algorithm of Egli (2013) was used to smooth the data with smoothing parameters of  $S_{c0}=4$ ,  $S_{b0}=3$ ,  $S_{c1}=S_{b1}=7$ .

FORC diagrams above the magnetic-mineral dissolution zone (1.00 and 1.14 m) have a sharp central ridge feature along the  $H_u=0$  axis, which indicates the contribution of non-interacting SD grains (Fig. 3a). This SD signature is interpreted to be of biogenic origin. The FORC diagrams also have broad vertical spread with an elliptical peak at a coercivity of 10–15 mT, and outer contours diverge from the  $H_u=0$  line toward the  $H_u$  axis. This component is considered to be carried by a mixture of interacting SD, vortex state, and multi-domain (MD) grains (Roberts et al. 2000, 2014, 2017; Lascau et al. 2018), which are interpreted to be of terrigenous origin. Collapsed chains of biogenic magnetite may also be included in this component (Li et al. 2012; Harrison and Lascau 2014). The contribution of the central ridge component decreases with depth within the dissolution zone, which is evident as a diminishing extracted central ridge signal with depth (Fig. 3b) and a downcore decrease of the proportion of the central ridge component to the broader, more vertically spread components on profiles along  $H_c=40$  mT (Fig. 3c) and along  $H_u=0$  (Fig. 3d). These observations indicate selective dissolution of biogenic magnetite. Coercivity distributions of both the biogenic and terrigenous components shift to lower values along with progressive reductive diagenesis (Fig. 3d); the peak coercivity of the biogenic component, initially ~45 mT, decreases to ~25 mT. This is probably due to decreasing grain volumes with dissolution. For the sample from the base of the dissolution zone at 1.49 m, vertical spread becomes somewhat narrower and the proportion of the central ridge component increases a little compared with the sample from 1.36 m.

## TEM observations

TEM observations provide a direct way to investigate biogenic magnetite in sediments, which is complementary to FORC measurements. Biogenic magnetite can be identified directly in TEM images from its characteristic morphologies (bullet shaped, hexagonal prisms, and octahedra) and uniform SD grain sizes (Bazylnski et al. 1994; Kopp and Kirschvink 2008). Particle morphology is not known from FORC distributions, although particle elongation may be estimated from coercivity distributions (Egli 2004; Yamazaki and Ikehara 2012; Usui et al. 2017; Yamazaki et al. 2020). The limitation of TEM observations is, on the other hand, that particle population under a TEM may not faithfully represent the original magnetic-mineral assemblage in a sample because magnetic-mineral extraction is required for observations. In this context, FORC distributions provide more quantitative information.

Magnetic minerals extracted from seven different depths in the core, 1.00, 1.14, 1.18, 1.23, 1.27, 1.36, and 1.49 m, were observed using a TEM. To extract magnetic minerals, sediments were first dispersed in distilled water with sodium hexametaphosphate using an ultrasonic bath, and magnetic minerals were then collected by circulating the dispersed sediments through a high magnetic-field gradient. The

magnetic extracts were dispersed in ethanol, and a small drop of the suspension was subsequently dried on a carbon-coated copper grid. A TEM (JEOL JEM-1400) at the Atmosphere and Ocean Research Institute, The University of Tokyo, operated at 120 kV, was used for the observations.

From morphologies seen in TEM images, magnetofossils were classified into three groups: bullet shaped, elongated, and equant (Fig. 4), although some ambiguity remains in estimating three-dimensional morphology from an image projected on a plane. The elongated group consists of hexagonal prisms and elongated octahedra. The equant group is represented by cubo-octahedra, although short hexagonal prisms with length/width ratios close to one are also included in this group. Bullet-shaped magnetofossils can be identified easily from their morphology. Relative abundances of biogenic magnetite from each morphological group and their grain-size distributions were obtained by counting several hundred grains in about 100 images for each sample. It should be noted that this kind of analysis remains semi-quantitative.

The sediments before reductive dissolution starts contain abundant magnetofossils of all three morphotypes (Fig. 4a), as reflected by the wide coercivity distribution along the central ridge of the FORC diagrams, from about 20 to 80 mT (Fig. 3). At the beginning of the reductive dissolution interval at 1.14 m, most of the biogenic magnetite has sharp crystal edges with little sign of dissolution in TEM images (Fig. 4b). However, some bullet-shaped magnetofossils have wavy crystal surfaces (Fig. 4c, arrows), which are indicative of partial dissolution. For the samples from 1.18 and 1.23 m, at which dissolution is underway (Fig. 2), many crystals are partially etched (Figs. 4d–4g). It is often observed that the caps of hexagonal prisms, which are constituted by {111} faces (Mann 1985; Meldrum et al. 1993), are etched while side faces are almost intact (Figs. 4d, and 4f). The wavy corrosion also affects bullet-shaped magnetofossils (Fig. 4e). Corroded equant magnetofossils have rounded shapes in general, which suggests that octahedral edges are corroded (Figs. 4g and 4h). In the lower part of the dissolution interval at 1.27 m, the characteristic morphologies of biogenic magnetite are almost lost (Figs. 4i and 4j), although some particles are inferred to be of biogenic origin from their sizes within or near the SD range. At 1.36 and 1.49 m near the base of the dissolution interval, no magnetofossil remains. Some grains that resemble silicate-hosted magnetic inclusions (Chang et al. 2016a; Zhang et al. 2018) are observed (Figs. 4k and 4l).

Length/width distributions for each morpho-type of magnetofossils determined in TEM images at four depths above and within the dissolution zone are shown in Fig. 5. Bullet-shaped magnetofossils are lost before others, and magnetofossils of the elongated group are most resistant to reductive dissolution. The proportion of the bullet-shaped group is ~40% before dissolution starts, and decreases to 14% at 1.23 m. On the other hand, the proportion of the elongated group increases from 38 to 63%.

## Discussion

FORC diagrams and TEM observations presented here reveal that biogenic magnetite dissolves preferentially in the interval between ~1.15 and 1.5 m in core GH98-1232, where magnetic-mineral

dissolution was previously estimated from a rapid magnetic-mineral concentration decrease with an average grain-size increase. Biogenic magnetite generally has smaller grain size and hence higher surface area to volume ratio than magnetic minerals of terrigenous origin, which is presumably responsible for the earlier dissolution of biogenic magnetite. Magnetite may also occur as inclusions within silicate minerals (Figs. 4k and 4l) and be protected from reductive dissolution (Chang et al. 2016a; Zhang et al. 2018; Usui et al. 2018). This contributes to the relative loss and preferential dissolution of biogenic magnetite with respect to detrital magnetite. In low-temperature measurements, the temperature of the maximum gradient in thermal decay curves of SIRM imparted at 6 K increases downcore from ~106 K to 118 K at about 1.5 m (Fig. 11 of Yamazaki et al. 2003), which is close to the depth of magnetofossil disappearance. This indicates the usefulness of the method proposed by Chang et al. (2016b) for discriminating biogenic magnetite from the detrital counterpart using the Verwey transition temperature. The narrower vertical spread in the FORC diagram and the remaining central-ridge component at the base of the dissolution zone at 1.49 m (Fig. 3) may be explained by the presence of silicate-hosted magnetic mineral inclusions, which are resistant to dissolution. The inclusions would have smaller magnetostatic interactions compared with aggregated bare terrigenous magnetites, which were mostly dissolved by this depth. The rebound of the average magnetic grain size observed in  $k_{ARM}/SIRM$  (Fig. 2b) may also be explained by the silicate-hosted magnetic inclusions; their grain sizes could be smaller than bare terrigenous magnetites.

This study reveals that resistance to reductive dissolution depends on magnetofossil morphology. With progressive reductive dissolution, the proportion of bullet-shaped magnetofossils decreases whereas that of elongated magnetofossils, which mainly consist of hexagonal prisms, increases. Because of the short dissolution interval of ~0.35 m, changes of biogenic magnetite production associated with variations in sediment environments should be small. This is supported by the similarity of the proportions of individual morpho-types above (1.00 m) and at the top (1.14 m) of the dissolution interval (Fig. 5).

The morphological dependence of magnetofossil dissolution can be explained by differences of crystallographic planes in magnetite and their different susceptibility to reductive dissolution. Allen et al. (1988) reported that among the (111), (110), and (100) planes of magnetite, the dissolution rate in a reducing agent is the largest for the (111) plane and smallest for the (110) plane, and the difference is more than a factor of two. The difference was inferred to be due to that the (111) plane presents a solution a close-packed array of oxygen atoms, which would be easily protonated under the acid conditions (Allen et al. 1988). Hexagonal prisms elongate in the [111] direction with {111} caps and {110} side faces (Mann 1985; Meldrum et al. 1993). The observations of TEM images from this study that {111} caps of hexagonal prisms are often etched whereas {110} side faces are almost intact are consistent with the (111) plane being the most vulnerable to dissolution. Equant octahedral magnetofossils have eight {111} faces that are truncated by apexes with {100} faces (Mann et al. 1984). For bullet-shaped magnetite, a variety of crystal growth has been reported, but the development of {110} faces is limited (Mann et al. 1987; Lefèvre et al. 2011; Li et al. 2015, 2020). Thus, hexagonal prismatic magnetofossils have larger proportions of resistant {110} faces in their surfaces compared to equant octahedral and

bullet-shaped magnetofossils. Furthermore, bullet-shaped magnetofossils have smaller axial ratios, then have higher surface area to volume ratios than other morpho-types, which presumably leads also to the larger decrease of bullet-shaped magnetofossils with progressive reductive dissolution.

The morphology of magnetite produced by magnetotactic bacteria (MTB) is considered to be specific to phylum- or class-level lineages (Bazylinski et al. 1994; Kopp and Kirschvink 2008; Lefèvre and Bazylinski 2013), or may be even species specific (Li et al. 2020). Recent magnetic and microbiological studies have suggested that bullet-shaped magnetofossils are preferentially found in the oxic-anoxic transition zone (OATZ), which are produced by MTB of Nitrospirae lineage, whereas hexagonal prismatic and octahedral magnetofossils are distributed both above and within the OATZ (Yamazaki et al. 2019; Nakano et al. submitted). Thus, magnetofossil morphology in sediments can be used as a proxy for past OATZ (Usui et al. 2017; Yamazaki et al. 2020). However, when applying in reducing sedimentary environments (Rodelli et al. 2019), care is needed because of possible alteration of the original magnetofossil morphological compositions in the dissolution process.

## Conclusions

Biogenic magnetite particles with hexagonal prismatic, bullet-shaped, and octahedral morpho-types are abundant in the studied sediment core from the Japan Sea. When they undergo reductive diagenesis, bullet-shaped magnetofossils dissolve earlier than the other two morpho-types, whereas hexagonal prisms are the most resistant to dissolution. This observation can be explained by differences in resistance among crystal planes against reductive dissolution and differences in surface area to volume ratios. When magnetofossil morphology is used as a proxy for paleoenvironments, care is needed to ensure that interpretation is not biased by possible alteration of original magnetofossil morphological compositions during reductive diagenesis.

## Abbreviations

AIST: National Institute of Advanced Industrial Science and Technology, ARM: Anhysteretic remanent magnetization, FORC: First-order reversal curve, GSJ: Geological Survey of Japan, MD: multi domain, MTB: magnetotactic bacteria, OATZ: oxic-anoxic transition zone, SD: single domain, SIRM: Saturation isothermal remanent magnetization, TEM: Transmission electron microscope

## Declarations

**Ethics approval and consent to participate**

**Not applicable**

**Consent for publication**

**Not applicable**

## Availability of data and materials

The data presented in Figs. 2 and 5 are included in Additional files 1 and 2, respectively. Raw FORC measurements and TEM images are available from the author on request.

## Competing interests

The author declares that he has no competing interests.

## Funding

This work was supported by JSPS KAKENHI Grant Numbers 16K13896, 18K18789, and 19H01997.

## Authors' contribution

TY designed the project, conducted the measurements, and wrote the manuscript.

## Acknowledgements

I thank Nobuhiro Ogawa for his assistance with TEM observations. I also thank Andrew Roberts, Liao Chang, and an anonymous reviewer for constructive comments, which greatly improved the manuscript. FORC measurements were conducted when I was an employee of GSJ, AIST.

## References

1. Allen GC, Kirby C, Sellers RM (1988) The effect of the low-oxidation state metal ion reagent tris-picolinatovanadium (II) formate on the surface morphology and composition of crystalline iron oxides. *J Chem Soc Faraday Trans 1* 84:355–364
2. Bazylinski DA, Garratt-Reed AJ, Frankel RB (1994) Electron microscopic studies on magnetosomes in magnetotactic bacteria. *Microsc Res Tech* 27:389–401
3. Canfield DE, Berner RA (1987) Dissolution and pyritization of magnetite in anoxic marine sediments. *Geochim Cosmochim Acta* 51:645–659
4. Chang L, Roberts AP, Winklhofer M, Heslop D, Dekkers MJ, Krigsman W, Fitz Gerald JD, Smith P (2014) Magnetic detection and characterization of biogenic magnetic minerals: a comparison of ferromagnetic resonance and first-order reversal curve diagrams. *J Geophys Res Solid Earth* 119:6136–6158
5. Chang L, Roberts AP, Heslop D, Hayashida A, Li J, Zhao X, Tian W, Huang Q (2016a) Widespread occurrence of silicate-hosted magnetic mineral inclusions in marine sediments and their contribution to paleomagnetic recording. *J Geophys Res Solid Earth* 121:8415–8431. doi:10.1002/2016JB013109
6. Chang L, Heslop D, Roberts AP, Rey D, Mohamed KJ (2016b) Discrimination of biogenic and detrital magnetite through a double Verwey transition temperature. *J Geophys Res Solid Earth* 121:3–14.

doi:10.1002/2015JB012485

7. Chang L, Harrison RJ, Zeng F, Berndt TA, Roberts AP, Heslop D, Zhao X (2018) Coupled microbial bloom and oxygenation decline recorded by magnetofossils during the Palaeocene–Eocene Thermal Maximum. *Nat Com* 9:4007. doi:10.1038/s41467-018-06472-y
8. Chen L, Heslop D, Roberts AP, Chang L, Zhao X, McGregor HV, Marino G, Rodriguez-Sanz L, Rohling EJ, Pälike H (2017) Remanence acquisition efficiency in biogenic and detrital magnetite and recording of geomagnetic paleointensity. *Geochem Geophys Geosyst* 18:1435–1450. doi:10.1002/2016GC006753
9. Egli R (2004) Characterization of individual rock magnetic components by analysis of remanence curves. 2. Fundamental properties of coercivity distributions. *Phys Chem Earth* 29:851–867
10. Egli R (2013) VARIFORC: An optimized protocol for calculating non-regular first-order reversal curve (FORC) diagrams. *Glob Planet Change* 110:302–320
11. Egli R, Chen AP, Winklhofer M, Kodama KP, Horng CS (2010) Detection of noninteracting single domain particles using first-order reversal curve diagrams. *Geochem Geophys Geosyst* 11:Q01Z11. doi:10.1029/2009GC002916
12. Harrison RJ, Feinberg JM (2008) FORCinel: An improved algorithm for calculating first-order reversal curve distributions using locally weighted regression smoothing. *Geochem Geophys Geosyst* 9:Q05016. doi:10.1029/2008GC001987
13. Harrison RJ, Lascu I (2014) FORCulator: A micromagnetic tool for simulating first-order reversal curve diagrams. *Geochem Geophys Geosyst* 15:4671–4691
14. Hesse PP (1994) Evidence for bacterial palaeoecological origin of mineral magnetic cycles in oxic and sub-oxic Tasman Sea sediments. *Mar Geol* 117:1–17
15. Karlin R (1990) Magnetite diagenesis in marine sediments from the Oregon continental margin. *J Geophys Res* 95:4405–4419.
16. Karlin R, Levi S (1983) Diagenesis of magnetic minerals in recent haemipelagic sediments. *Nature* 303:327–330
17. Kirschvink JL (1982) Paleomagnetic evidence for fossil biogenic magnetite in western Crete. *Earth Planet Sci Lett* 59:388–392
18. Korff L, von Dobeneck T, Frederichs T, Kasten S, Kuhn G (2016) Cyclic magnetite dissolution in Pleistocene sediments of the abyssal northwest Pacific Ocean: Evidence for glacial oxygen depletion and carbon trapping. *Paleoceanography* 31:600–624. doi:10.1002/2015PA002882
19. Kopp RE, Kirschvink JL (2008) The identification and biogeochemical interpretation of fossil magnetotactic bacteria. *Earth-Sci Rev* 86:42–61
20. Lascu I, Einsle JF, Ball MR, Harrison RJ (2018) The vortex state in geologic materials: A micromagnetic perspective. *J Geophys Res Solid Earth* 123:7285–7304. doi:10.1029/2018JB015909
21. Lefèvre CT, Pósfai M, Abreu F, Lins U, Frankel RB, Bazylinski DA (2011) Morphological features of elongated-anisotropic magnetosome crystals in magnetotactic bacteria of the *Nitrospirae* phylum

and the *Deltaproteobacteria* Earth Planet Sci Lett 312:194–200

22. Lefèvre CT, Bazylinski DA (2013) Ecology, diversity, and evolution of magnetotactic bacteria. *Microbiol Mol Biol Rev* 77:497–526
23. Li J, Wu W, Liu Q, Pan Y (2012) Magnetic anisotropy, magnetostatic interactions and identification of magnetofossils. *Geochem Geophys Geosyst* 13:Q10Z51. doi:10.1029/2012GC004384
24. Li J, Menguy N, Gatel C, Boureau V, Snoeck E, Patriarche G, Leroy E, Pan Y (2015) Crystal growth of bullet-shaped magnetite in magnetotactic bacteria of the *Nitrospirae* *J R Soc Interface* 12:20141288. doi:10.1098/rsif.2014.1288
25. Li J, Menguy N, Roberts AP, Gu L, Leroy E, Bourgon J, Yang X, Zhao X, Liu P, Changela HG, Pan Y (2020) Bullet-shaped magnetite biomineralization within a magnetotactic Deltaproteobacterium: Implications for magnetofossil identification. *J Geophys Res Biogeosci* 125:e2020JG005680. doi:10.1029/2020JG005680
26. Mann S (1985) Structure, morphology, and crystal growth of bacterial magnetite. In: Kirschvink JL, Jones DS, MacFadden BJ (eds) *Magnetite biomineralization and magnetoreception in organisms*, Plenum, New York, pp 311–332
27. Mann S, Frankel RB, Blakemore RP (1984) Structure, morphology and crystal growth of bacterial magnetite. *Nature* 310:405–407
28. Mann S, Sparks NHC, Blakemore RP (1987) Structure, morphology and crystal growth of anisotropic magnetite crystals in magnetotactic bacteria. *Proc R Soc Lond B* 231:477–487
29. Meldrum FC, Mann S, Heywood BR, Frankel RB, Bazylinski DA (1993) Electron microscopy study of magnetosomes in a cultured coccoid magnetotactic bacteria. *Proc R Soc Lond B* 251:231–236
30. Muxworthy AR, Williams W (2009) Critical superparamagnetic/single-domain grain sizes in interacting magnetite particles: implications for magnetosome crystals. *J R Soc Interface* 6:1207–1212. doi:10.1098/rsif.2008.0462
31. Nakano S, Furutani H, Kato S, Kouduka M, Yamazaki T, Suzuki Y, Coupling of Nitrospirae-affiliated genomic profiles to teardrop magnetosomes in deep-sea environments. *Environ Microbiol Rep*, submitted
32. Ouyang T, Heslop D, Roberts AP, Tian C, Zhu Z, Qiu Y, Peng X (2014) Variable remanence acquisition efficiency in sediments containing biogenic and detrital magnetites: Implications for relative paleointensity signal recording. *Geochem Geophys Geosyst* 15:2780–2796. doi:10.1002/2014GC005301
33. Pike CR, Roberts AP, Verosub KL (1999) Characterizing interactions in fine magnetic particle systems using first order reversal curves. *J Appl Phys* 85:6660–6667
34. Roberts AP (2015) Magnetic mineral diagenesis. *Earth-Sci Rev* 151:1–47
35. Roberts AP, Pike CR, Verosub KL (2000) First-order reversal curve diagrams: A new tool for characterizing the magnetic properties of natural samples. *J Geophys Res* 105:28461–28475

36. Roberts AP, Florindo F, Villa G, Chang L, Jovane L, Bohaty SM, Larrasoaña JC, Heslop D, Fitz Gerald JD (2011) Magnetotactic bacterial abundance in pelagic marine environments is limited by organic carbon flux and availability of dissolved iron. *Earth Planet Sci Lett* 310:441–452
37. Roberts AP, Chang L, Heslop D, Florindo F, Larrasoaña JC (2012) Searching for single domain magnetite in the “pseudo-single domain” sedimentary haystack: Implications of biogenic magnetite preservation for sediment magnetism and relative paleointensity determinations. *J Geophys Res* 117:B08104. doi:10.1029/2012JB009412
38. Roberts AP, Florindo F, Chang L, Heslop D, Jovane L, Larrasoaña JC (2013) Magnetic properties of pelagic marine carbonate. *Earth-Sci Rev* 127:111–139
39. Roberts AP, Heslop D, Zhao X, Pike CR (2014) Understanding fine magnetic particle systems through use of first-order reversal curve diagrams. *Rev Geophys* 53:557–602. doi:10.1002/2014RG000462
40. Roberts AP, Almeida TP, Church NS, Harrison RJ, Heslop D, Li Y, Li J, Muxworthy AR, Williams W, Zhao X (2017) Resolving the origin of pseudo-single domain magnetic behavior. *J Geophys Res Solid Earth* 122:9534–9558. doi:10.1002/2017JB014860
41. Rodelli D, Jovane L, Giorgioni M, Rego ES, Cornaggia F, Benites M, Cedraz P, Berbel GBB, Braga ES, Ustra A, Abreu F, Roberts AP (2019) Diagenetic fate of biogenic soft and hard magnetite in chemically stratified sedimentary environments of Mamanguá Ría, Brazil. *J Geophys Res Solid Earth* 124:2313–2330. doi:10.1029/2018JB016576
42. Rowan CJ, Roberts AP, Broadbent T (2009) Reductive diagenesis, magnetite dissolution, greigite growth and paleomagnetic smoothing in marine sediments: A new view. *Earth Planet Sci Lett* 277:223–235
43. Usui Y, Yamazaki T, Saitoh M (2017) Changing abundance of magnetofossil morphologies in pelagic red clay around Minamitorishima, western North Pacific. *Geochem Geophys Geosyst* 18:4558–4572
44. Usui Y, Shimono T, Yamazaki T (2018) Rock magnetism of quartz and feldspars chemically separated from pelagic red clay: a new approach to provenance study. *Earth Planets Space* 70:133. doi:10.1186/s40623-018-0918-1
45. Yamazaki T, and Kawahata H (1998) Organic carbon flux controls the morphology of magnetofossils in marine sediments. *Geology* 26:1064–1066
46. Yamazaki T, Ikehara M (2012) Origin of magnetic mineral concentration variation in the Southern Ocean. *Paleoceanography* 27:PA2206. doi:10.1029/2011PA002271
47. Yamazaki T, Shimono T (2013) Abundant bacterial magnetite occurrence in oxic red clay. *Geology* 41:1191–1194
48. Yamazaki T, Abdeldayem AL, Ikehara K (2003) Rock-magnetic changes with reduction diagenesis in Japan Sea sediments and preservation of geomagnetic secular variation in inclination during the last 30,000 years. *Earth Planets Space* 55:327–340
49. Yamazaki T, Suzuki Y, Kouduka M, Kawamura N (2019) Dependence of bacterial magnetosome morphology on chemical conditions in deep-sea sediments. *Earth Planet Sci Lett* 513:135–143

50. Yamazaki T, Fu W, Shimono T, Usui Y (2020) Unmixing biogenic and terrigenous magnetic mineral components in red clay of the Pacific Ocean using principal component analyses of first-order reversal curve diagrams and paleoenvironmental implications. *Earth Planets Space* 72:120. doi:10.1186/s40623-020-01248-5
51. Zhang Q, Liu Q, Li J, Sun Y (2018) An integrated study of the eolian dust in pelagic sediments from the North Pacific Ocean based on environmental magnetism, transmission electron microscopy, and diffuse reflectance spectroscopy. *J Geophys Res Solid Earth* 123:3358–3376

## Figures

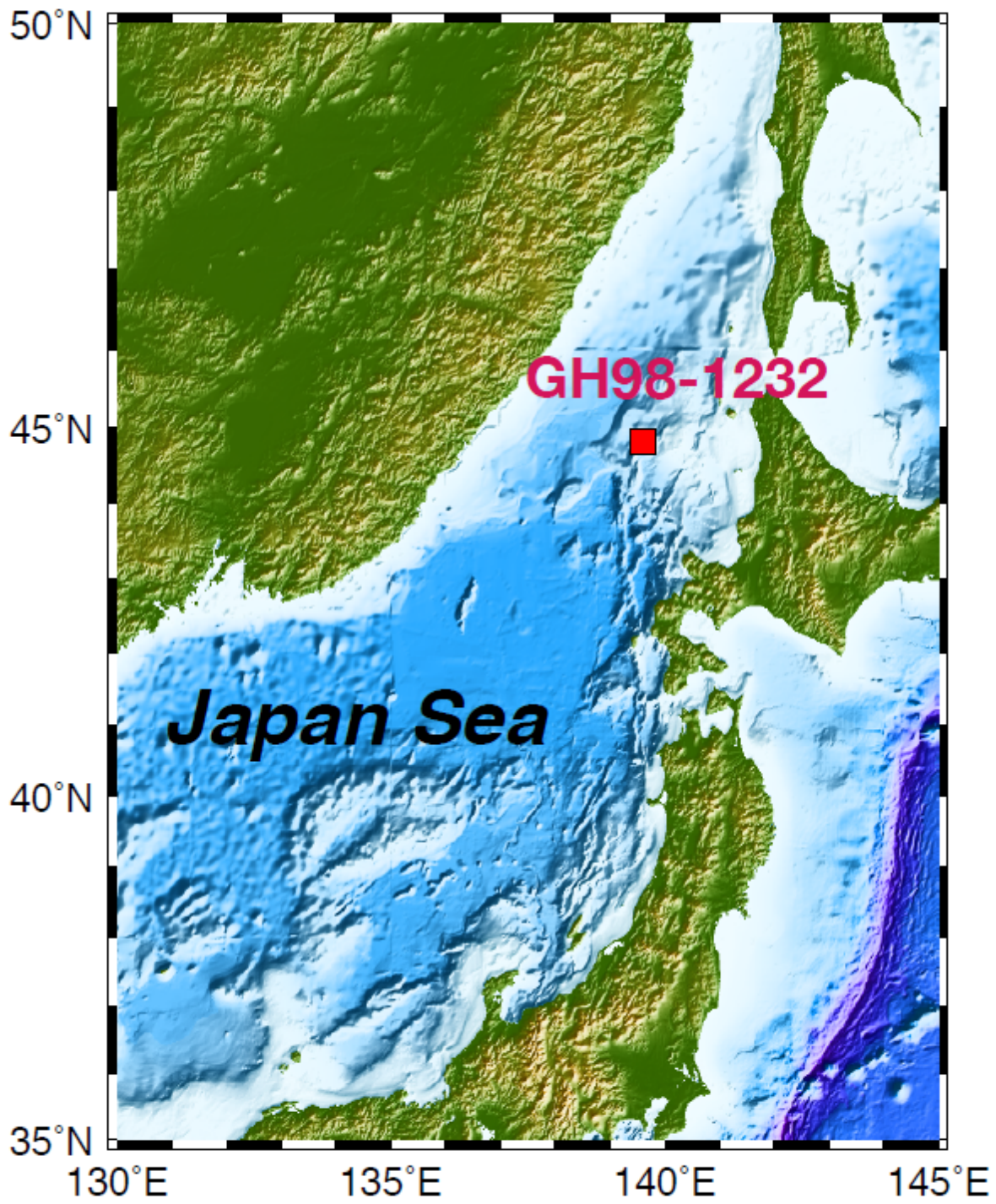


Figure 1

Location of the studied core in the Japan Sea.

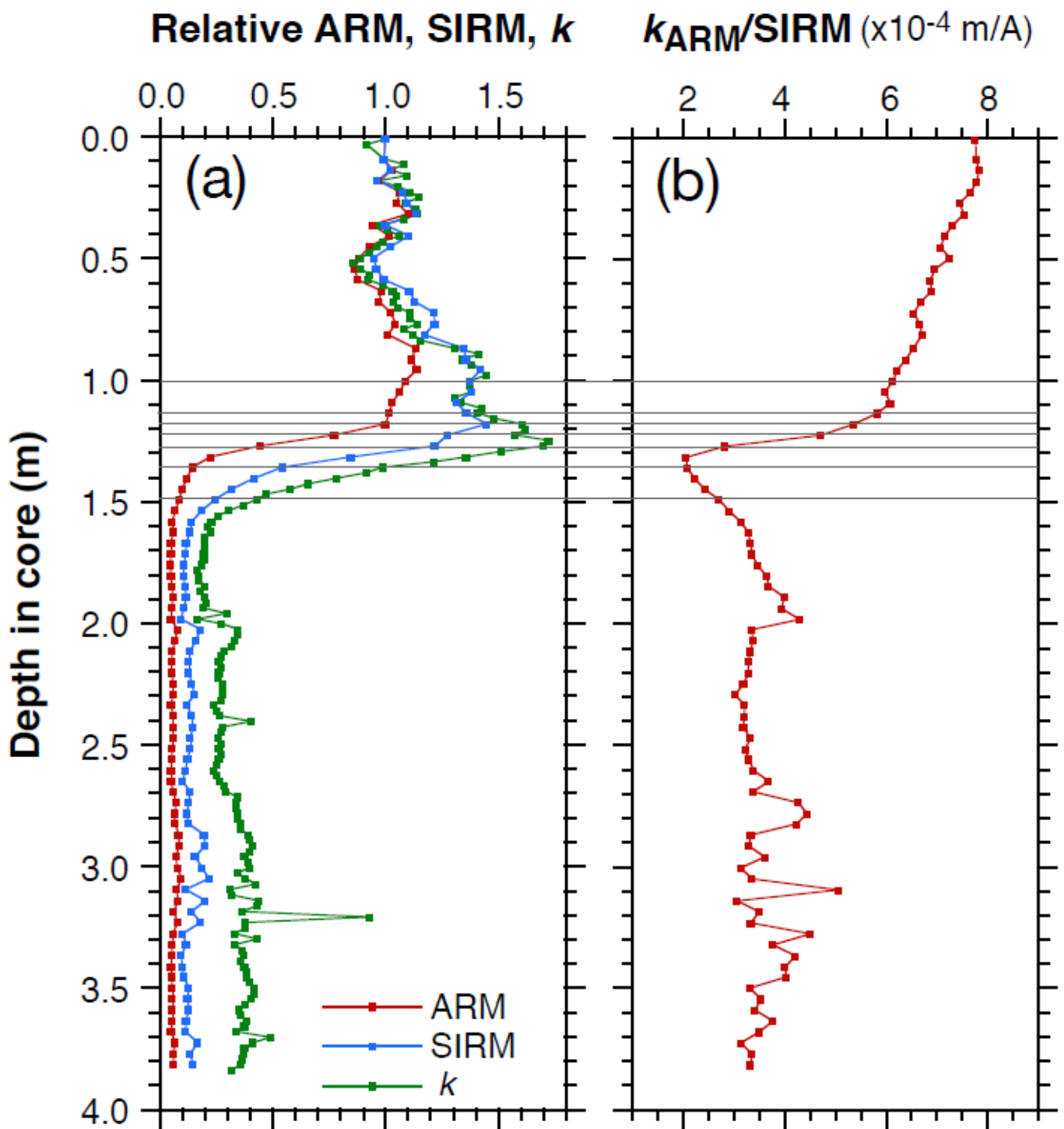
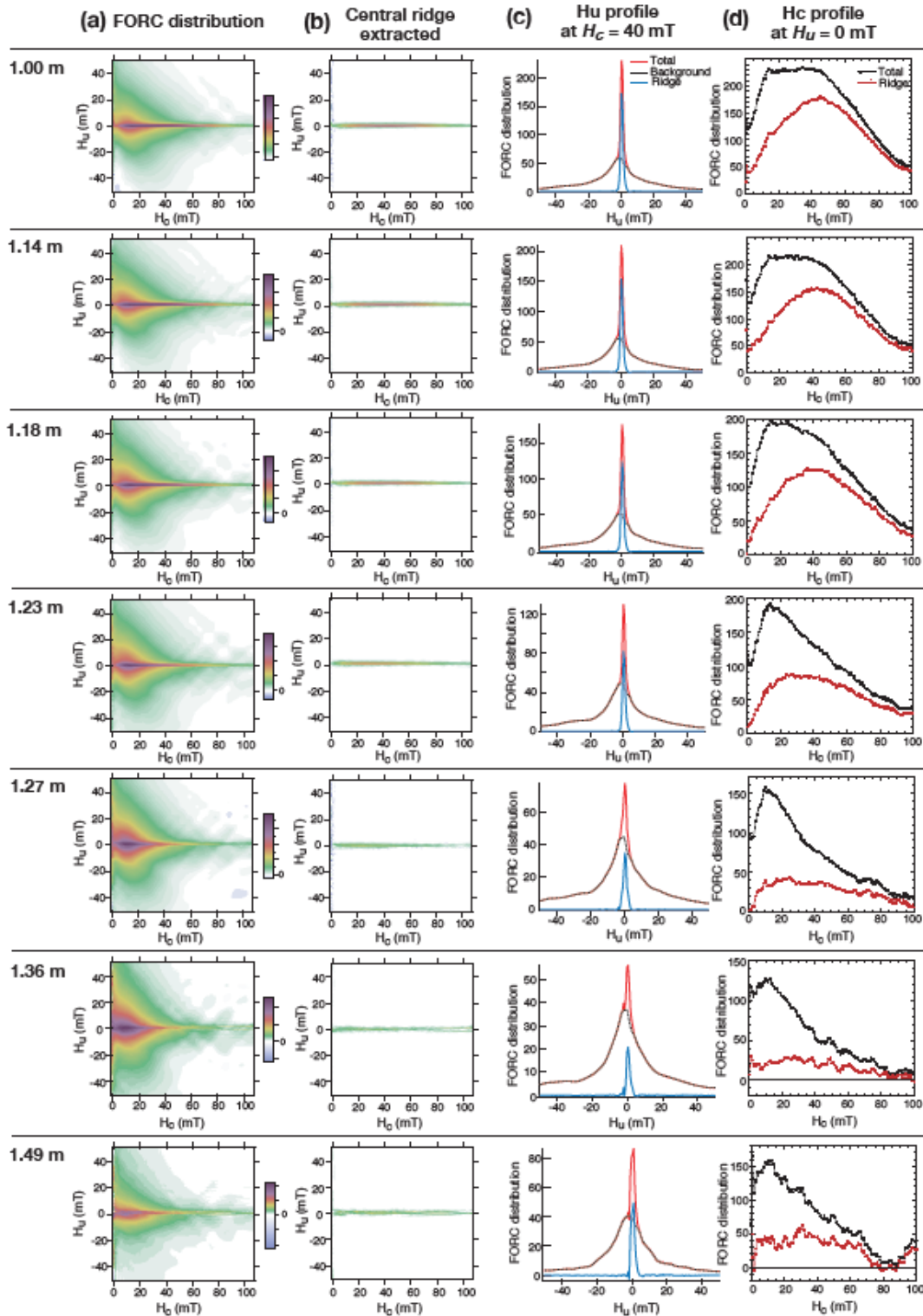


Figure 2

Variations of magnetic-mineral concentration and grain size with depth in core GH98-1232. (a) Relative variations of anhysteretic remanent magnetization (ARM) (red), saturation isothermal remanent magnetization (SIRM) (green), and magnetic susceptibility ( $k$ ) after Yamazaki et al. (2003). (b) The ratio of ARM susceptibility ( $k_{ARM}$ ) to SIRM. Smaller ratios are interpreted to be indicative of larger

average magnetic grain sizes. Thin horizontal lines indicate depth horizons for samples for which datasets are shown in Figs. 3 and 4.



**Figure 3**

First-order reversal curve (FORC) results of samples from seven depth horizons shown in Fig. 2, indicating (a) FORC diagrams, (b) the central ridge component extracted from the respective FORC diagrams, (c) profiles of magnetostatic-interaction field ( $H_u$ ) distributions at a coercivity ( $H_c$ ) of 40 mT: the central-

ridge component (blue), the background component with vertical spread (black), and the total of the two (red), and (d) profiles of coercivity distributions at zero interaction field ( $H_u=0$ ): the central-ridge component (red) and the total (black).

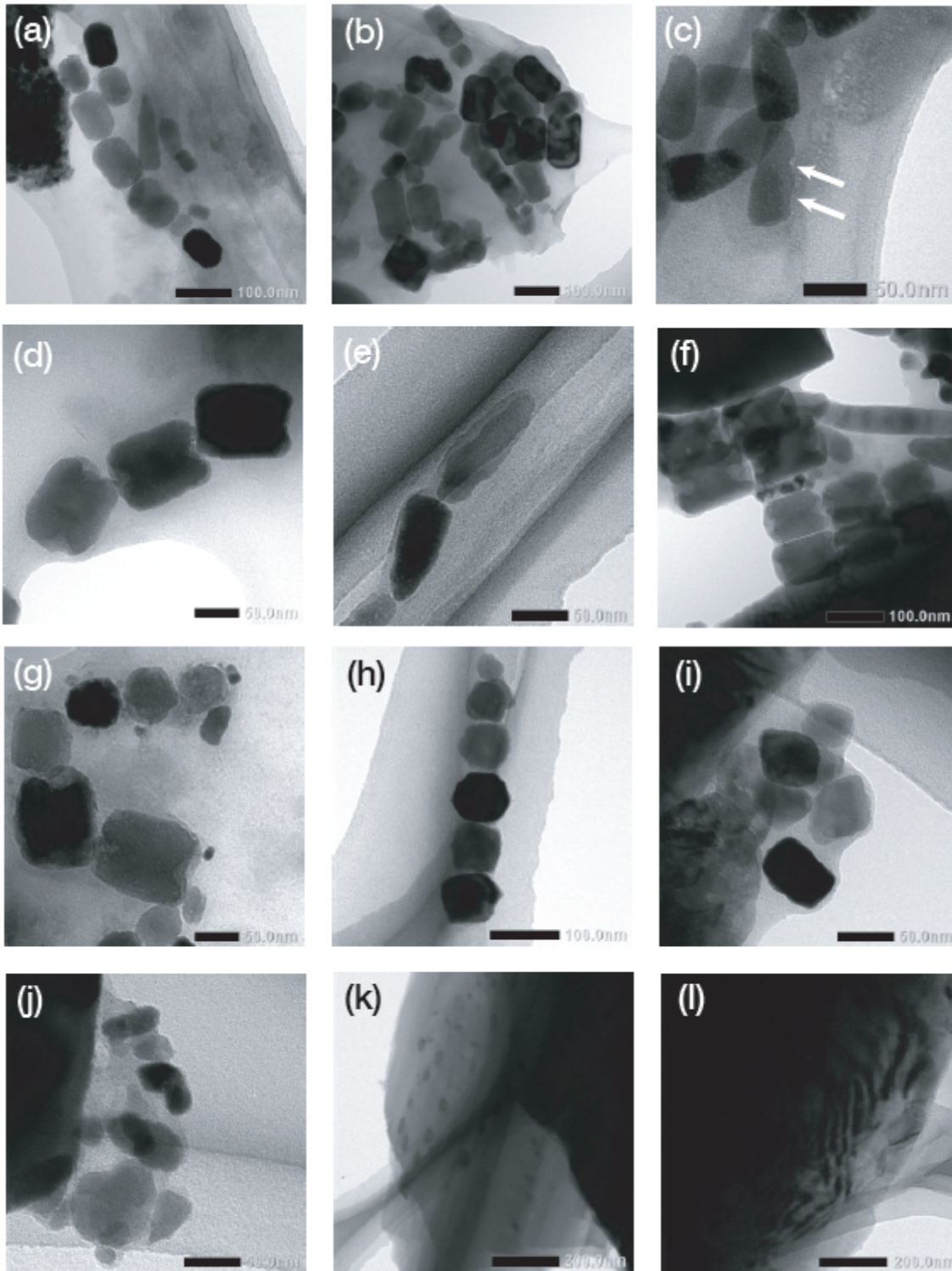


**Figure 4**

Transmission electron microscope (TEM) images of magnetic extracts from seven depth horizons shown in Fig. 2. Samples from (a) 1.00 m, (b, c) 1.14 m, (d–f) 1.18 m, (g, h) 1.23 m, (i, j) 1.27 m, (k) 1.36 m, and

(l) 1.49 m. Scale bar: 50 nm (c–e, g, i, j), 100 nm (a, b, f, h), and 200 nm (k, l).

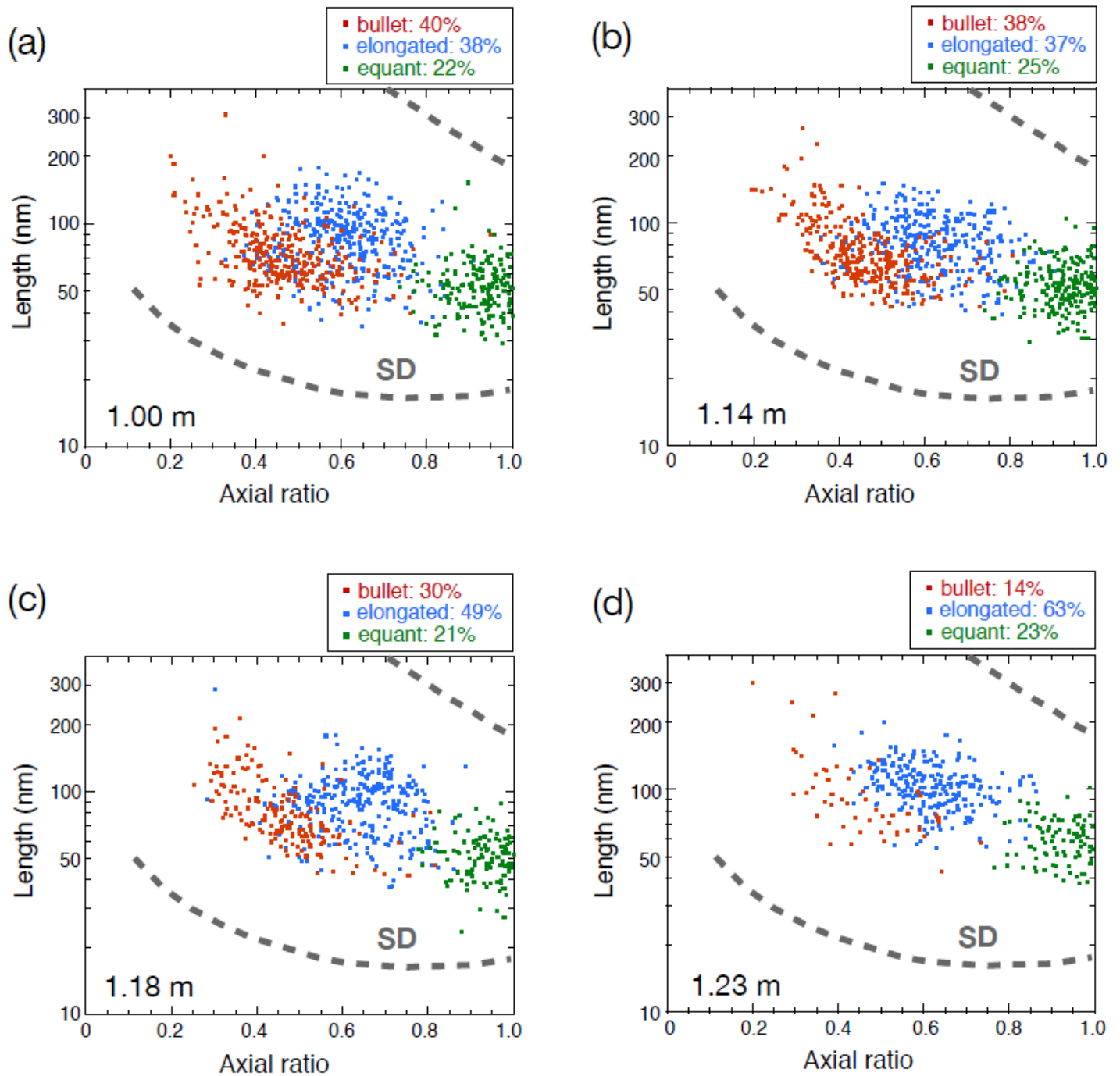


**Figure 5**

Morphology and grain size of magnetofossils with respect to magnetic domain state. Samples are depths of (a) 1.00 m, (b) 1.14 m, (c) 1.18 m, and (d) 1.23 m in the core. Magnetofossils are categorized into the three groups based on their morphology: bullet-shaped (red), elongated (blue), and equant (green). Bold dashed curves indicate the maximum single-domain (SD) region for chains of magnetite particles with magnetostatic interactions after Muxworthy and Williams (2009).

## Supplementary Files

This is a list of supplementary files associated with this preprint. Click to download.

- [Fig2data.xls](#)
- [Fig5data.xls](#)
- [GraphicabstractR1.pdf](#)